Coupling chromatin structure and dynamics by live super-resolution imaging

Barth, R.; Bystricky, K.; Shaban, H. A.

Important note
To cite this publication, please use the final published version (if applicable).
Please check the document version above.

CELL BIOLOGY

Coupling chromatin structure and dynamics by live super-resolution imaging

R. Barth[1,2], K. Bystricky[1,3], H. A. Shaban[1,4]*†

Chromatin conformation regulates gene expression and thus, constant remodeling of chromatin structure is essential to guarantee proper cell function. To gain insight into the spatiotemporal organization of the genome, we use high-density photoactivated localization microscopy and deep learning to obtain temporally resolved super-resolution images of chromatin in living cells. In combination with high-resolution dense motion reconstruction, we find elongated ~45- to 90-nm-wide chromatin "blobs." A computational chromatin model suggests that these blobs are dynamically associating chromatin fragments in close physical and genomic proximity and adopt topologically associated domain–like interactions in the time-average limit. Experimentally, we found that chromatin exhibits a spatiotemporal correlation over ~4 μm in space and tens of seconds in time, while chromatin dynamics are correlated over ~6 μm and last 40 s. Notably, chromatin structure and dynamics are closely related, which may constitute a mechanism to grant access to regions with high local chromatin concentration.

INTRODUCTION

The three-dimensional organization of the eukaryotic genome plays a central role in gene regulation (*1*). Its spatial organization has been prominently characterized by molecular and cellular approaches including high-throughput chromosome conformation capture (Hi-C) (*2*) and fluorescent in situ hybridization (*3*). Topologically associated domains (TADs), genomic regions that display a high degree of interaction, were revealed and found to be a key architectural feature (*4*). Direct three-dimensional localization microscopy of the chromatin fiber at the nanoscale (*5*) confirmed the presence of TADs in single cells but also, among others, revealed great structural variation of chromatin architecture (*3*). To comprehensively resolve the spatial heterogeneity of chromatin, super-resolution microscopy must be used. Previous work showed that nucleosomes are distributed as segregated, nanometer-sized accumulations throughout the nucleus (*6*–*8*) and that the epigenetic state of a locus has a large impact on its folding (*9*, *10*). However, to resolve the fine structure of chromatin, high labeling densities, long acquisition times, and, often, cell fixation are required. This precludes capturing dynamic processes of chromatin in single live cells, yet chromatin moves at different spatial and temporal scales.

The first efforts to relate chromatin organization and its dynamics were made using a combination of photoactivated localization microscopy (PALM) and tracking of single nucleosomes (*11*). It could be shown that nucleosomes mostly move coherently with their underlying domains, in accordance with conventional microscopy data (*12*); however, a quantitative link between the observed dynamics and the surrounding chromatin structure could not yet be established in real time. Although it is becoming increasingly clear that chromatin motion and long-range interactions are key to genome organization and gene regulation (*13*), tools to detect and to define

bulk chromatin motion simultaneously at divergent spatiotemporal scales and high resolution are still missing.

Here, we apply deep learning–based PALM (Deep-PALM) for temporally resolved super-resolution imaging of chromatin in vivo. Deep-PALM acquires a single resolved image in a few hundred milliseconds with a spatial resolution of ~60 nm. We observed elongated ~45- to 90-nm-wide chromatin domain "blobs." Using a computational chromosome model, we inferred that blobs are highly dynamic entities, which dynamically assemble and disassemble. Consisting of chromatin in close physical and genomic proximity, our chromosome model indicates that blobs, nevertheless, adopt TAD-like interaction patterns when chromatin configurations are averaged over time. Using a combination of Deep-PALM and high-resolution dense motion reconstruction (*14*), we simultaneously analyzed both structural and dynamic properties of chromatin. Our analysis emphasizes the presence of spatiotemporal cross-correlations between chromatin structure and dynamics, extending several micrometers in space and tens of seconds in time. Furthermore, extraction and statistical mapping of multiple parameters from the dynamic behavior of chromatin blobs show that chromatin density regulates local chromatin dynamics.

RESULTS

Deep-PALM reveals dynamic chromatin remodeling in living cells

Super-resolution imaging of complex and compact macromolecules such as chromatin requires dense labeling of the chromatin fiber to resolve fine features. We use Deep-STORM, a method that uses a deep convolutional neural network (CNN) to predict super-resolution images from stochastically blinking emitters (Fig. 1A; see Materials and Methods) (*15*). The CNN was trained to specific labeling densities for live-cell chromatin imaging using a photoactivated fluorophore (PATagRFP); we therefore refer to the method as Deep-PALM. We chose three labeling densities 4, 6, and 9 emitters/μm^2 per frame in the ON-state to test on the basis of the comparison of simulated and experimental wide-field images (fig. S1A). The CNN trained with 9 emitters/μm^2 performed significantly worse than the other CNNs and was thus excluded from further analysis (fig. S1B; see Materials

[1]Laboratoire de Biologie Moléculaire Eucaryote (LBME), Centre de Biologie Intégrative (CBI), CNRS, University of Toulouse, UPS, 31062 Toulouse, France. [2]Department of Bionanoscience, Delft University of Technology, 2628 CJ, Delft, Netherlands. [3]Institut Universitaire de France (IUF), Paris, France. [4]Spectroscopy Department, Physics Division, National Research Centre, Dokki, 12622 Cairo, Egypt.
*Present address: Center for Advanced Imaging, Faculty of Arts and Sciences, Northwest Building, Harvard University, Cambridge, MA 02138, USA.
†Corresponding author. Email: h_shaban@g.harvard.edu
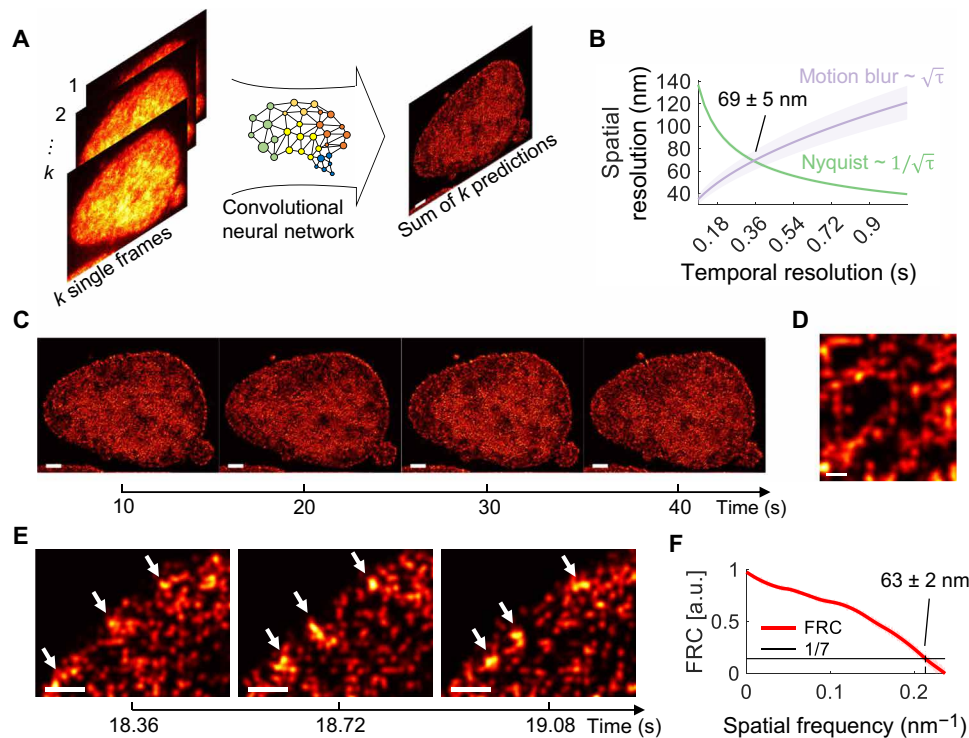
Fig. 1. Temporally resolved super-resolution images of chromatin in U2OS nuclei. (**A**) Wide-field images of U2OS nuclei expressing H2B-PATagRFP are input to a trained CNN, and predictions from multiple input frames are summed to construct a super-resolved image of chromatin in vivo. (**B**) The resolution trade-off between the prolonged acquisition of emitter localizations (green line) and motion blur due to diffusion of the underlying diffusion processes (purple line). For our experimental data, the localization density per second is $\rho = (2.4 \pm 0.1)\,\mu m^{-2} s^{-1}$, the diffusion constant is $D = (3.4 \pm 0.8) \cdot 10^{-3}\,\mu m^2 s^{-1}$ (see fig. S8B), and the acquisition time per frame is $\tau = 30$ ms. The spatial resolution assumes a minimum (69 ± 5 nm) at a time resolution of 360 ms. (**C**) Super-resolution images of a single nucleus at time intervals of about 10 s. Scale bars, 2 μm. (**D**) Magnification of segregated accumulations of H2B within a chromatin-rich region. Scale bar, 200 nm. (**E**) Magnification of a stable but dynamic structure (arrows) over three consecutive images. Scale bars, 500 nm. (**F**) Fourier ring correlation (FRC) for super-resolved images resulting in a spatial resolution of 63 ± 2 nm. FRC was conducted on the basis of 332 consecutive super-resolved images from two cells. a.u. arbitrary units.

and Methods). We applied Deep-PALM to reconstruct an image set of labeled histone protein (H2B-PATagRFP) in human bone osteosarcoma (U2OS) cells using the networks trained on 4 and 6 emitters/μm² per frame (see Materials and Methods). A varying number of predictions by the CNN of each frame of the input series were summed to reconstruct a temporal series of super-resolved images (fig. S1C). The predictions made by the CNN trained with 4 emitters/μm² show large spaces devoid of signal intensity, especially at the nuclear periphery, making this CNN inadequate for live-cell super-resolution imaging of chromatin. While collecting photons from long acquisitions for super-resolution imaging is desirable in fixed cells, Deep-PALM is a live imaging approach. Summing over many individual predictions leads to considerable motion blur and thus loss in resolution. Quantitatively, the Nyquist criterion states that the image resolution $R = 2/\sqrt{\tau \rho}$ depends on ρ, the localization density per second, and the time resolution τ (16). In contrast, motion blur strictly depends on the diffusion constant D of the underlying structure $R = \sqrt{4D\tau}$. There is thus an optimum resolution due to the trade-off between increased emitter sampling and the avoidance of motion blur, which was at a time resolution of 360 ms for our experiments (Fig. 1B and fig. S1D).

Super-resolution imaging of H2B-PATagRFP in live cells at this temporal resolution shows a pronounced nuclear periphery, while fluorescent signals in the interior vary in intensity (Fig. 1C). This likely corresponds to chromatin-rich and chromatin-poor regions

(8). These regions rearrange over time, reflecting the dynamic behavior of bulk chromatin. Chromatin-rich and chromatin-poor regions were visible not only at the scale of the whole nucleus but also at the resolution of a few hundred nanometers (Fig. 1D). Within chromatin-rich regions, the intensity distribution was not uniform but exhibited spatially segregated accumulations of labeled histones of variable shape and size, reminiscent of nucleosome clutches (6), nanodomains (9, 11), or TADs (17). At the nuclear periphery, prominent structures arise. Certain chromatin structures could be observed for ~1 s, which underwent conformational changes during this period (Fig. 1E). The spatial resolution at which structural elements can be observed (see Materials and Methods) in time-resolved super-resolution data of chromatin was 63 ± 2 nm (Fig. 1E), slightly more optimistic than the theoretical prediction (Fig. 1B) (18).

We compared images of H2B reconstructed from 12 frames (super-resolved images) by Deep-PALM in living cells to super-resolution images reconstructed by 8000 frames of H2B in fixed cells (fig. S2, A and B). Overall, the contrast in the fixed sample appears higher, and the nuclear periphery appears more prominent than in images from living cells. However, in accordance with the previous super-resolution images of chromatin in fixed cells (6, 8, 9, 11, 17) and Deep-PALM images, we observe segregated accumulations of signal throughout the nucleus. Thus, Deep-PALM identifies spatially heterogeneous coverage of chromatin, as previously reported (6, 8, 9, 11, 17). We further monitor chromatin temporally at the nanometer scale in living cells.

Chromatin appears in elongated nanometer-sized blobs with a nonrandom spatial distribution

To quantitatively assess the spatial distribution of H2B, we developed an image segmentation scheme (see Materials and Methods; fig. S3), which allowed us to segment spatially separated accumulations of H2B signal with high fidelity (note S1 and figs. S4 and S5). Applying our segmentation scheme, ~10,000 separable elements, blob-like structures were observed for each super-resolved image (166 resolved images per movie; Fig. 2A). The experimental resolution does not enable us to elucidate their origin and formation because tracking of blobs in three dimensions would be necessary to do so (see Discussion). We therefore turned to a transferable computational model introduced by Qi and Zhang (19), which is based on one-dimensional genomics and epigenomics data, including histone modification profiles and binding sites of CTCF (CCCTC-binding factor). To compare our data to the simulations, super-resolution images were generated
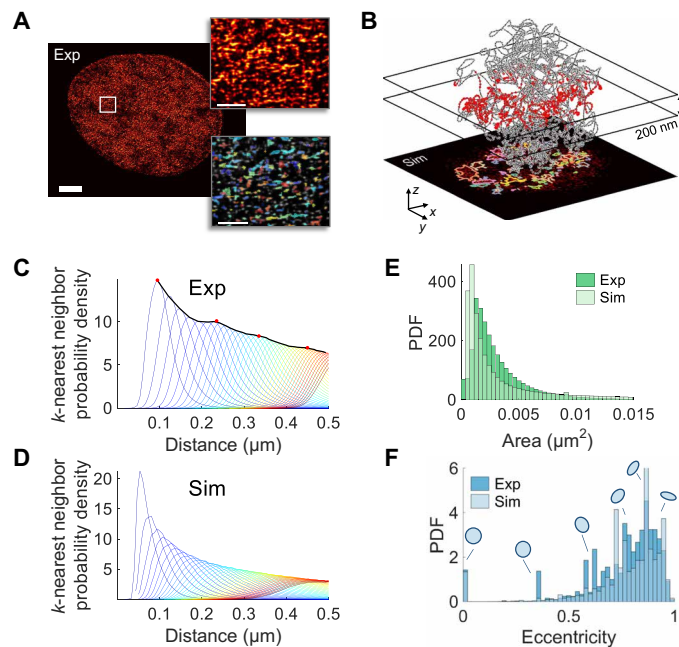
Fig. 2. Chromatin blob identification and characterization of imaged and modeled chromatin. (**A**) Super-resolved images show blobs of chromatin (left). These blobs are segmented (see Materials and Methods and note S1) and individually labeled by random color (right). Magnifications of the boxed regions are shown. Scale bars, 2 μm (whole nucleus); magnifications, 200 nm. (**B**) Generation of super-resolution images and blob identification and characterization for a 25–million base pair (Mbp) segment of chromosome 1 from GM12878 cells, as simulated in Qi and Zhang (19). Beads (5-kb genomic length) of a simulated polymer configuration within a 200-nm-thick slab are projected to the imaging plane, resembling experimental super-resolved images of live chromatin. Blobs are identified as on experimental data. (**C**) From the centroid positions, the NND distributions are computed for up to 40 nearest neighbors (blue to red). The envelope of the k-NND distributions (black line) shows peaks at approximately 95, 235, 335, and 450 nm (red dots). (**D**) k-NND distributions as in (B) for simulated data. (**E**) Area distribution of experimental and simulated blobs. The distribution is, in both cases, well described by a lognormal distribution with parameters (3.3 ± 2.8) × 10⁻³ μm² for experimental blobs and (3.1 ± 3.2) × 10⁻³ μm² for simulated blobs (means ± SD). PDF, probability density function. (**F**) Eccentricity distribution for experimental and simulated chromatin blobs. Selected eccentricity values are illustrated by ellipses with the corresponding eccentricity. Eccentricity values range from 0, describing a circle, to 1, describing a line. Prominent peaks arise because of the discretization of chromatin blobs in pixels. The data are based on 332 consecutive super-resolved images from two cells, in each of with ~10,000 blobs were identified.

from the modeled chromosomes. Within these images, we could identify and characterize "chromatin blobs" analogously to those derived from experimental data (see Materials and Methods; Fig. 2B).

For imaged (in living and fixed cells) and modeled chromatin, we first computed the kth nearest-neighbor distance (NND; centroid-to-centroid) distributions, taking into account the nearest 1st to 40th neighbors (Fig. 2C and fig. S2, C and D, blue to red). Centroids of the nearest neighbors are (95 ± 30) nm (means ± SD) apart, consistent with previous and our own super-resolution images of chromatin in fixed cells (9) and slightly further than what was found for clutches of nucleosomes (6). The envelope of all NND distributions (Fig. 2C, black line) shows several weak maxima at ~95, 235, 335, and 450 nm, which roughly coincide with the peaks of the 1st, 7th, 14th, and 25th nearest neighbors, respectively (Fig. 2C, red dots). In contrast, simulated data exhibit a prominent first nearest-neighbor peak at a slightly smaller distance, and higher-order NND distribution decay quickly and appear washed out (Fig. 2D). This hints toward greater levels of spatial organization of chromatin in vivo, which is not readily recapitulated in the used state-of-the-art chromosome model.

Next, we were interested in the typical size of chromatin blobs. Their area distribution (Fig. 2E) fit a log-normal distribution with parameters (3.3 ± 2.8) × 10⁻³ μm² (means ± SD), which is in line with the area distribution derived from fixed samples (fig. S2E) and modeled chromosomes. Notably, blob areas vary considerably, as indicated by the high SD and the prominent tail of the area distribution toward large values. Following this, we calculated the eccentricity of each blob to resolve their shape (Fig. 2F and fig. S2F). The eccentricity is a measure of the elongation of a region reflecting the ratio of the longest chord of the shape and the shortest chord perpendicular to it (Fig. 2F; illustrated shapes at selected eccentricity values). The distribution of eccentricity values shows an accumulation of values close to 1, with a peak value of ~0.9, which shows that most blobs have an elongated, fiber-like shape and are not circular. In particular, the eccentricity value of 0.9 corresponds to a ratio between the short and long axes of the ellipse of 1:2 (see Materials and Methods), which results, considering the typical area of blobs in experimental and simulated data, in roughly 92-nm-long and 46-nm-wide blobs on average. A highly similar value was found in fixed cells (fig. S2F). The length coincides with the value found for the typical NND [Fig. 2C; (95 ± 30) nm]. However, because of the segregation of chromatin into blobs, their elongated shape, and their random orientation (Fig. 2A), the blobs cannot be closely packed throughout the nucleus. We find that chromatin has a spatially heterogeneous density, occupying 5 to 60% of the nuclear area (fig. S6, A and B), which is supported by a previous electron microscopy study (20).

Blob dimensions derived from live-cell super-resolution imaging using Deep-PALM are consistent with those found in fixed cells, thereby further validating our method, and in agreement with previously determined size ranges (6, 9). A previously published chromosome model based on Hi-C data (and thus not tuned to display blob-like structures per se) also displays blobs with dimensions comparable to those found here, in living cells. Together, these data strongly suggest the existence of spatially segregated chromatin structures in the sub–100-nm range.

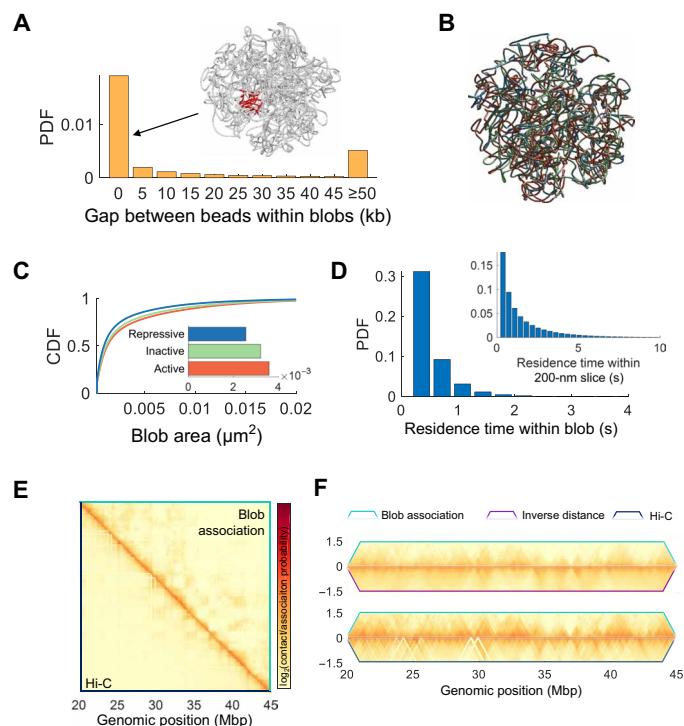## Chromatin blobs identified by Deep-PALM are coherent with sub-TADs

The simulations offer to track each monomer (chromatin locus) unambiguously, which is currently not possible to do from experimental

data. Since the simulations show blobs comparable to those found in experiment (Fig. 2), simulations help to indicate possible mechanisms leading to the observation of chromatin blobs. For instance, because of the projection of the nuclear volume onto the imaging plane, the observed blobs could simply be overlays of distant, along the one-dimensional genome, noninteracting genomic loci. To examine this possibility, we analyzed the gap length between beads belonging to the same blob along the simulated chromosome. Beads constitute the monomers of the simulated chromosome, and each bead represents roughly 5 kb (*19*).

The analysis showed that the blobs are mostly made of consecutive beads along the genome, thus implying an underlying domain-like structure, similar to TADs (Fig. 3A). Using the affiliation of each

Fig. 3. Chromatin blobs on modeled chromosomes consist of continuous loci along the genome and exhibit a TAD-like time-averaged conformation. (**A**) Gap length between beads belonging to the same blob. An exemplary blob with small gap length is shown. The blob is mostly made of consecutive beads being in close spatial proximity. (**B**) A representative polymer configuration is colored according to chromatin states (red, active; green, inactive; and blue, repressive). (**C**) The cumulative distribution function (CDF) of clusters within active, inactive, and repressive chromatin. Inset: Mean area of clusters within the three types of chromatin. The distributions are all significantly different from each other, as determined by a two-sample Kolmogorov-Smirnov test ($P < 10^{-50}$). (**D**) Distribution of the continuous residence time of any monomer within a cluster (0.5 ± 0.3 s; means $\pm$ SD). Inset: Continuous residence time of any monomer within a slab of 200-nm thickness (1.5 ± 1.6 s; means $\pm$ SD). (**E**) The blob association strength between any two beads is measured as the frequency at which any two beads are found in one blob. The association map is averaged over all simulated configurations (upper triangular matrix; from simulations), and experimental Hi-C counts are shown for the same chromosome segment [lower triangular matrix; from Rao *et al.* (*40*)]. The association and Hi-C maps are strongly correlated [Pearson's correlation coefficient (PCC) = 0.76]. (**F**) Close-up views around the diagonal of Hi-C–like matrices. The association strength is shown together with the inverse distance between beads (top; PCC = 0.85) and with experimental Hi-C counts [bottom; as in (E)]. The data are based on 20,000 polymer configurations.

bead to an intrinsic chromatin state of the model (Fig. 3B), it became apparent that blobs along the simulated chromosome consisting mostly of active chromatin are significantly larger than those formed by inactive and repressive chromatin (Fig. 3C). These findings are in line with experimental results (*10*) and results from the simulations directly (*19*), thereby validating the projection and segmentation process.

Since chromatin is dynamic in vivo and in computer simulations, each bead can diffuse in and out of the imaging volume from frame to frame. We estimated that, on average, each bead spent approximately 1.5 s continuously within a slab of 200-nm thickness (Fig. 3D). Furthermore, a bead is, on average, found only 0.55 ± 0.33 s continuously within a blob, which corresponds to one to two experimental super-resolved images (Fig. 3D). These results suggest that chromatin blobs are highly dynamic entities, which usually form and dissemble within less than 1 s. We thus constructed a time-averaged association map for the modeled chromosomes, quantifying the frequency at which each locus is found with any other locus within one blob. The association map is comparable to interaction maps derived from Hi-C (Fig. 3E). Notably, interlocus association and Hi-C maps are strongly correlated, and the association map shows similar patterns as those identified as TADs in Hi-C maps, even for relatively distant genomic loci [>1 million base pairs (Mbp)]. A similar TAD-like organization is also apparent when the average inverse distance between loci is considered (Fig. 3F, top), suggesting that blobs could be identified in super-resolved images because of the proximity of loci within blobs in physical space. The computational chromosome model indicates that chromatin blobs identified by Deep-PALM are mostly made of continuous regions along the genome and cannot be attributed to artifacts originating from the projection of the three-dimensional genome structure to the imaging plane. The simulations further indicate that the blobs associate and dissociate within less than 1 s, but loci within blobs are likely to belong to the same TAD. Their average genomic content is 75 kb, only a fraction of typical TAD lengths in mammalian cells (average size, 880 kb) (*4*), suggesting that blobs likely correspond to sub-TADs or TAD nanocompartments (*17*).

Quantitative chromatin dynamics at nanoscale resolution

To quantify the experimentally observed chromatin dynamics at the nanoscale, down to the size of one pixel (13.5 nm), we used a dense reconstruction of flow fields, optical flow (Fig. 4A; see Materials and Methods), which was previously used to analyze images taken on confocal (*12*, *14*), and structured illumination microscopes (*8*). We examined the suitability of optical flow for super-resolution on the basis of single-molecule localization images using simulations. We find that the accuracy of optical flow is slightly enhanced on super-resolved images compared to conventional fluorescence microscopy images (note S2 and fig. S7, A to C). Experimental super-resolution flow fields are illustrated on the basis of two subsequent images, between which the dynamics of structural features are apparent to the eye (fig. S7, D and E). On the nuclear periphery, connected regions spanning up to ~500 nm can be observed [fig. S7D (i and ii), marked by arrows]. These structures are stable for at least 360 ms but move from frame to frame. The flow field is shown on top of an overlay of the two super-resolved images and color-coded [fig. S7D (iii); the intensity in frame 1 is shown in green, the intensity in frame 2 is shown in purple, and colocalization of both is white]. Displacement vectors closely follow the redistribution of
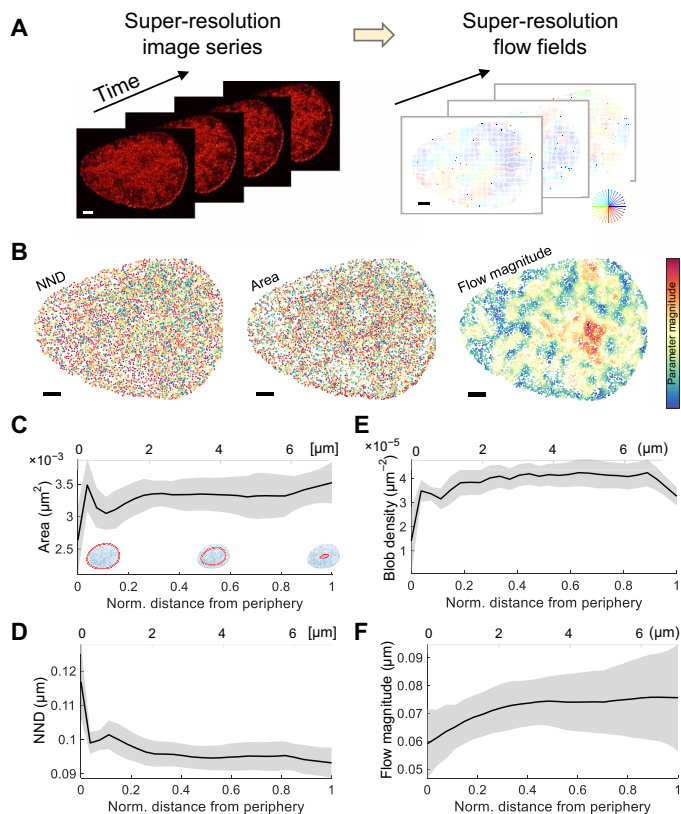
Fig. 4. Structural and dynamics blob characteristics dependent on the proximity to the nuclear periphery. (**A**) A time series of super-resolution images (left) is subject to optical flow (right). (**B**) Blobs of a representative nucleus (see movie S1) are labeled by their NND (left), area (middle), and flow magnitude (right). Colors denote the corresponding parameter magnitude. (**C**) The average blob area, (**D**) NND, (**E**) density, and (**F**) flow magnitude are shown versus the normalized distance from the nuclear periphery (lower x axis; 0 is on the periphery and 1 is at the center of the nucleus) and versus the absolute distance (upper x axis). Line and shaded area denote the means ± SE from 322 super-resolved images of two cells. Scale bar, (A) and (B): 3 μm.

intensity from frame to frame (roughly from green to purple). Similarly, structures within the nuclear interior (fig. S7E) can be followed by eye, thus further validating and justifying the use of a dense motion reconstruction as a quantification tool of super-resolved chromatin motion.

Using optical flow fields, we linked the spatial appearance of chromatin to their dynamics. Effectively, the blobs were characterized with two structural parameters (NND and area) and their flow magnitude (Fig. 4B). Movie S1 shows the time evolution of those parameters for an exemplary nucleus. Blobs at the nuclear periphery showed a distinct behavior from those in the nuclear interior. In particular, the periphery exhibits a lower density of blobs, but those appear slightly larger and are less mobile than in the nuclear interior (Fig. 4, C to F), in line with previous findings using conventional microscopy (*14*). The peripheral blobs are reminiscent of dense and relatively immobile heterochromatin and lamina-associated domains (*21*), which extend only up to 0.5 μm inside the nuclear interior. In contrast, blob dynamics increase gradually within 1 to 2 μm from the nuclear rim.

Chromatin structure and dynamics are linked

To further elucidate the relationship between chromatin structure and dynamics, we analyzed the correlation between each pair of parameters in space and time. Therefore, we computed the auto- and

cross-correlation of parameter maps with a given time lag across the entire nucleus (in space) (Fig. 5A). In general, a positive correlation denotes a low-low or a high-high relationship (a variable de-/increases when another variable de-/increases), while, analogously, a negative correlation denotes a high-low relationship. The autocorrelation of NND maps [Fig. 5A (i)] shows a positive correlation; thus, regions exist spanning 2 to 4 μm, in which chromatin is either closely packed (low-low) or widely dispersed (high-high). Likewise, blobs of similar size tend to be in spatial proximity [Fig. 5A (iii)]. These regions are not stable over time but rearrange continuously, an observation bolstered by the fact that the autocorrelation diminishes with increasing time lag. The cross-correlation between NND and area [Fig. 5A (ii)] shows a negative correlation for short time lags, suggesting that large blobs appear with a high local density while small ones are more isolated. The correlation becomes slightly positive for time lags ≥20 s, indicating that big blobs are present in regions that were sparsely populated before and small blobs tend to accumulate in previously densely populated regions. This is in line with dynamic reorganization and reshaping of chromatin domains on a global scale, as observed in snapshots of the Deep-PALM image series (Fig. 1A).

The flow magnitude is positively correlated for all time lags, while the correlation displays a slight increase for time lags ≤20 s [Fig. 5A (vi)], which has also been observed previously (*8, 12, 22*). The spatial autocorrelation of dynamic and structural properties of chromatin are in stark contrast. While structural parameters are highly correlated at short but not at long time scales, chromatin motion is still correlated at a time scale exceeding 30 s. At very short time scales (<100 ms), stochastic fluctuations determine the local motion of the chromatin fiber, while coherent motion becomes apparent at longer times (*22*). However, there exists a strong cross-correlation between structural and dynamic parameters: The cross-correlation between the NND and flow magnitude shows notable negative correlation at all time lags [Fig. 5A (iv)], strongly suggesting that sparsely distributed blobs appear less mobile than densely packed ones. The area seems to play a negligible role for short time lags, but there is a modest tendency that regions with large blobs tend to exhibit increased dynamics at later time points [≥10 s; Fig. 5A (v)], likely due to the strong relationship between area and NND.

In general, parameter pairs involving chromatin dynamics exhibit an extended spatial auto- or cross-correlation (up to ~6 μm; the lower row of Fig. 5A) compared to correlation curves including solely structural parameters (up to 3 to 4 μm). Furthermore, the cross-correlation of flow magnitude and NND does not considerably change for increasing time lag, suggesting that the coupling between those parameters is characterized by an unexpectedly resilient memory, lasting for at least tens of seconds (*23*). Concomitantly, the spatial correlation of time-averaged NND maps and maps of the local diffusion constant of chromatin for the entire acquisition time enforces their negative correlation at the time scale of ~1 min (fig. S8). Such resilient memory was also proposed by a computational study that observed that interphase nuclei behave similar to concentrated solutions of unentangled ring polymers (*24*). Our data support the view that chromatin is mostly unentangled since entanglement would influence the anomalous exponent of genomic loci in regions of varying chromatin density (*24*). However, our data do not reveal a correlation between the anomalous exponent and the time-averaged chromatin density (fig. S8), in line with our previous results using conventional microscopy (*14*).
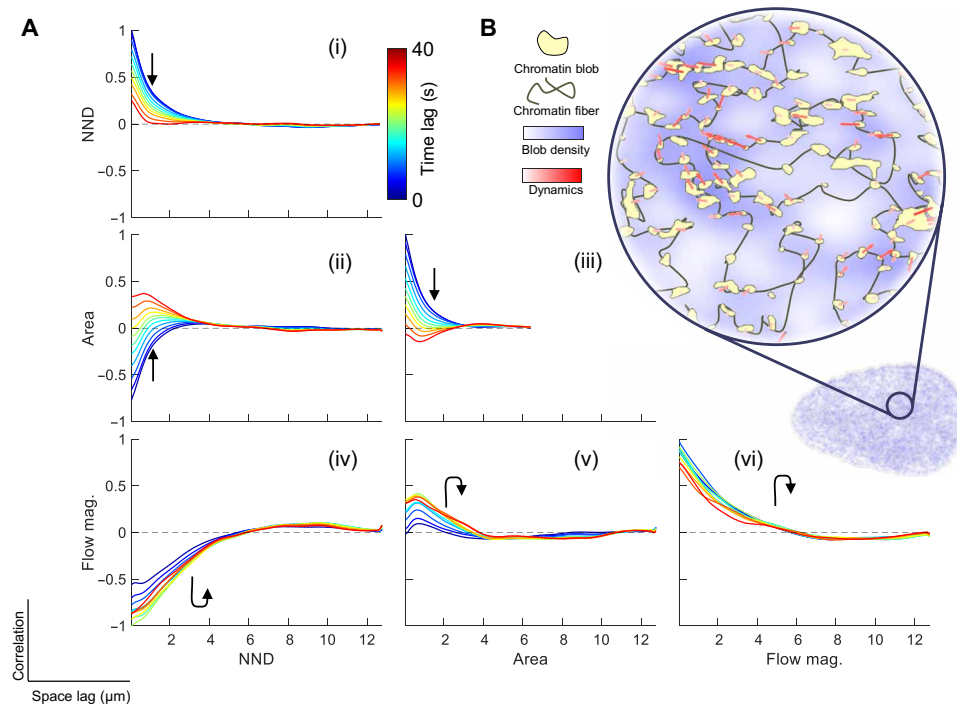
Fig. 5. Spatiotemporal correlations between structural and dynamic parameters. (**A**) The spatial auto- and cross-correlation between parameters were computed for different time lags. The graphs depict the correlation over space lag for each parameter pair, and different colors denote the time lag (increasing from blue to red). (**B**) Illustration of the instantaneous relationship between local chromatin density and dynamics. The blob density is shown in blue; the magnitude of chromatin dynamics is shown by red arrows. The consistent negative correlation between NND and flow magnitude is expressed by increased dynamics in regions of high local blob density. Data represent the average over two cells. The cells behave similarly such that error bars are omitted for the sake of clarity.

Overall, the spatial cross-correlation between chromatin structure and dynamics indicates that the NND between blobs and their mobility stand in a strong mutual, negative relationship. This relationship, however, concerns chromatin density variations at the nanoscale, but not global spatial density variations such as in euchromatin or heterochromatin (*14*). These results support a model in which regions with high local chromatin density, i.e., larger blobs are more prevalent and are mobile, while small blobs are sparsely distributed and less mobile (Fig. 5B). Blob density and dynamics in the long-time limit are, to an unexpectedly large extent, influenced by preceding chromatin conformations.

The local chromatin density is a key regulator of instantaneous chromatin dynamics

The spatial correlations above were only evaluated pairwise, while the behavior of every blob is likely determined by a multitude of factors in the complex energy landscape of chromatin (*19, 22*). Here, we aim to take a wider range of available information into account to reveal the principle parameters, driving the observed chromatin structure and dynamics. Using a microscopy-based approach, we have access to a total of six relevant structural, dynamic, and global parameters, which potentially shape the chromatin landscape in space and time (Fig. 6A). In addition to the parameters used above, we included the confinement level as a relative measure, allowing the quantification of transient confinement (see Materials and Methods). We further included the bare signal intensity of super-resolved images and, as the only static parameter, the distance from the periphery since it was shown that dynamic and structural parameters

show some dependence on this parameter (Fig. 4). We then used *t*-distributed stochastic neighbor embedding (*t*-SNE) (*25*), a state-of-the-art dimensionality reduction technique, to map the six-dimensional chromatin "features" (the six input parameters) into two dimensions (Fig. 6A and see note S3). The *t*-SNE algorithm projects data points such that neighbors in high-dimensional space likely stay neighbors in two-dimensional space (*25*). Visually apparent grouping of points (Fig. 6B) implies that grouped points exhibit great similarity with respect to all input features, and it is of interest to reveal which subset of the input features can explain the similarity among chromatin blobs best. It is likely that points appear grouped because their value of a certain input feature is considerably higher or lower than the corresponding value of other data points. We hence labeled points in *t*-SNE maps which are smaller than the first quartile point or larger than the third quartile point. Data points falling in either of the low/high partition of one input feature are colored accordingly for visualization (Fig. 6D; blue/red points, respectively). We then assigned a rank to each of the input features according to their nearest-neighbor fraction (n-n fraction): Since the *t*-SNE algorithm conserves nearest neighbors, we described the extent of grouping in *t*-SNE maps by the fraction of nearest neighbors, which fall in either one of the subpopulations of low or high points (illustrated in fig. S9). A high n-n fraction (Fig. 6C) therefore indicates that many points marked as low/high are indeed grouped by *t*-SNE and are therefore similar. The ranking (from low to high n-n fraction) reflects the potency of a given parameter to induce similar behavior between chromatin blobs with respect to all input features.
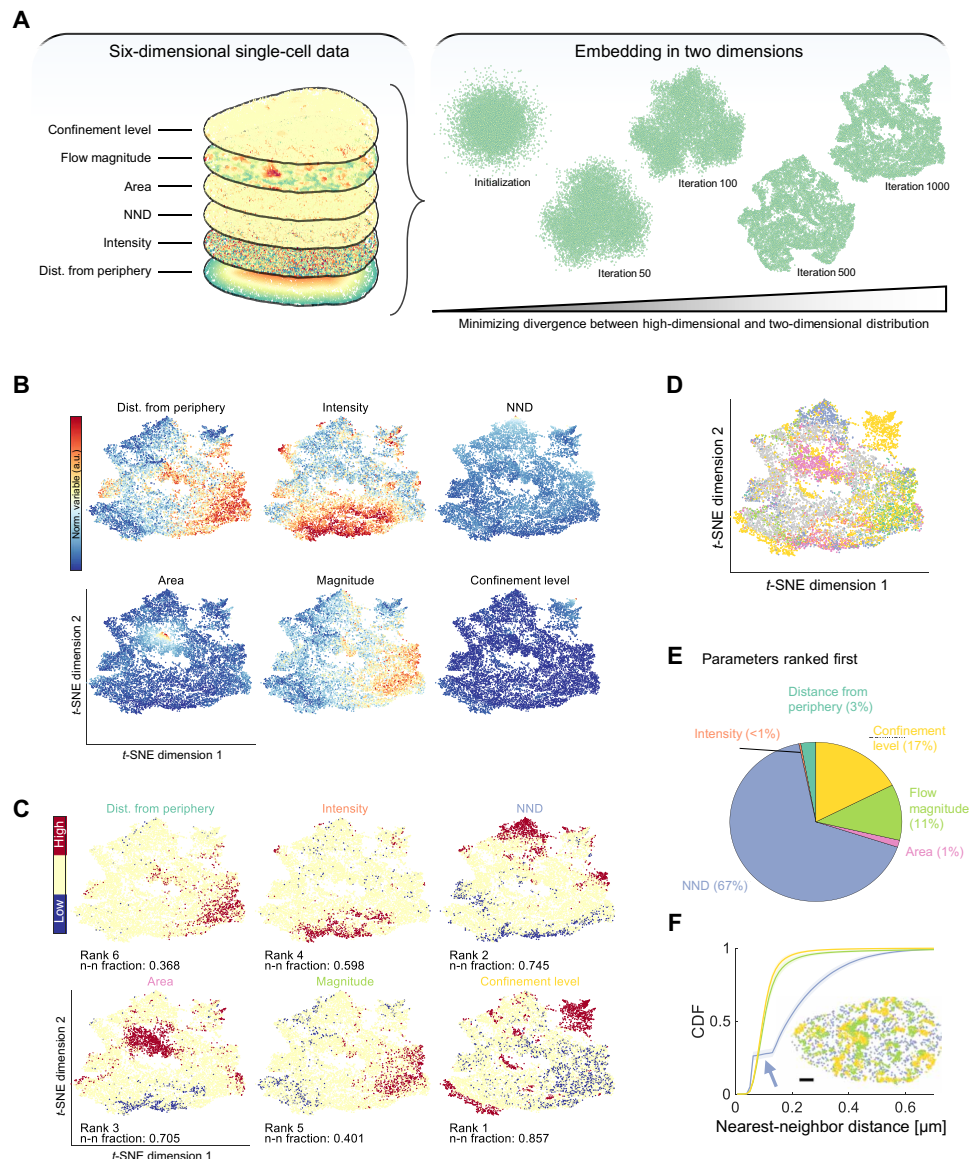
Fig. 6. Chromatin feature extraction. (**A**) The six-dimensional parameter space is input to the *t*-SNE algorithm and projected to two dimensions. (**B**) The two-dimensional embedding of an exemplary dataset is shown and colored according to the magnitude of each input feature (blue to red; the parameter average is shown in beige). (**C**) Points below the first (blue) and above the third (red) quartile points of the corresponding parameter are marked, and the parameters are ranked according to the fraction of nearest neighbors that fall in one of the marked regions. (**D**) Data points marked below the first or above the third quartile points are labeled according to the feature in which they were marked. Priority is given to the feature with the higher n-n fraction if necessary. (**E**) *t*-SNE analysis is carried out for each nucleus over the whole time series, and it is counted how often a parameter ranked first. The results are visualized as a pie chart. The NND predominantly ranks first in about two-thirds of all cases. (**F**) Marked points in (C) and (D) are mapped back onto the corresponding nuclei, and the CDF over space is shown (means ± SE). Pie chart and CDF computations are based on 322 super-resolved images from two cells.

The relative frequency at which each parameter ranked first provides an intuitive feeling for the most "influential" parameters in the dataset (Fig. 6E). The signal intensity plays a negligible role, suggesting that our data are free of potential artifacts related to the bare signal intensity. Furthermore, the blob area and the distance from the periphery likewise do not considerably shape chromatin blobs. In contrast, the NND between blobs was found to be the main factor inducing the observed characteristics in 67% of all-time frames across all nuclei. The flow magnitude and confinement level together rank first in 26% of all cases (11 and 17%, respectively). These

numbers suggest that the local chromatin density is a universal key regulator of instantaneous chromatin dynamics. Note that no temporal dependency is included in the *t*-SNE analysis and, thus, the feature extraction concerns only short-term (≤360 ms) relationships. The characteristics of roughly one-fourth of all blobs at each time point are mainly determined by similar dynamical features. Mapping chromatin blobs as marked in Fig. 6 (C and D) back to their respective positions inside the nucleus (Fig. 6F) shows that blobs with low/high flow magnitude or confinement level markedly also grouped in physical space, which is highly reminiscent of coherent

motion of chromatin (*12*). In contrast, blobs with extraordinary low or high NND were found interspersed throughout the nucleus, in line with spatial correlation analysis between structural and dynamic features (Fig. 5). Our results point toward a large influence of the local chromatin density on the dynamics of chromatin at the scale of a few hundred nanometers and within a few hundred milliseconds. At longer time and length scales, however, previous results suggest that this relationship is lost (*14*).

DISCUSSION

With Deep-PALM, we present temporally resolved super-resolution images of chromatin in living cells. Our technique identified chromatin nanodomains, named blobs, which mostly have an elongated shape, consistent with the curvilinear arrangement of chromatin, as revealed by structured illumination microscopy (*8*) with typical axes lengths of 45 to 90 nm. A previous study reported ~30-nm-wide "clutches of nucleosomes" in fixed mammalian cells using STORM nanoscopy (*6*), while the larger value obtained using Deep-PALM may be attributed to the motion blurring effect in live-cell imaging. However, histone acetylation and methylation marks were shown to form nanodomains of diameter 60 to 140 nm, respectively (*9*), which includes the computed dimensions for histone H2B using Deep-PALM.

To elucidate the origin of chromatin blobs, we turned to a simulated chromosome model, which displays chromatin blobs similar to our experimental data when seen in a super-resolution reconstruction. The simulations suggest that chromatin blobs consist of continuous genomic regions with an average length of 75 kb, assembling and disassembling dynamically within less than 1 s. Monomers within blobs display a distinct TAD-like association pattern in the long-time limit, suggesting that the identified blobs represent sub-TADs. Transient formation is consistent with recent findings that TADs are not stable structural elements but exhibit extensive heterogeneity and dynamics (*3*, *5*). To experimentally probe the transient assembly of chromatin blobs, it would be interesting to track individual blobs over time. However, this is a nontrivial task. While the size (area/volume) or shape of blobs could be used to establish correspondences between blobs in subsequent frames, the framework needs to be flexible enough to allow for blob deformations since blobs likely arise stochastically and are not rigid bodies. Achieving an even shorter acquisition time per frame in the future could help minimize the influence of blob deformations and make tracking feasible. The second challenge is to distinguish between disassembly and out-of-focus diffusion of a blob. The three-dimensional imaging at sufficient spatial and temporal resolution will be helpful in the future to overcome this hurdle.

Using an optical flow approach to determine the blob dynamics instead, we found that structural and dynamic parameters exhibit extended spatial and temporal (cross-) correlations. Structural parameters such as the local chromatin density (expressed as the NND between blobs) and area lose their correlation after 3 to 4 μm and roughly 40 s in the spatial and temporal dimension, respectively. In contrast, chromatin mobility correlations extend over ~6 μm and persist during the whole acquisition period (≥40 s). Extensive spatiotemporal correlation of chromatin dynamics has been presented previously, both experimentally (*12*) and in simulations (*22*), but was not linked to the spatiotemporal behavior of the underlying chromatin structure until now. We found that the chromatin dynamics are closely linked to the instantaneous but also to past local structural characterization of chromatin. In other words, the instantaneous local chromatin density influences chromatin dynamics in the future and vice versa. On the basis of these findings, we suggest that chromatin dynamics exhibit an extraordinary long memory. This strong temporal relationship might be established by the fact that stress propagation is affected by the folded chromosome organization (*26*). Fiber displacements cause structural reconfiguration, ultimately leading to a local amplification of chromatin motion in local high-density environments. This observation is also supported by the fact that increased nucleosome mobility grants chromatin accessibility even within regions of high nucleosome density (*27*).

Given the persistence at which correlations of chromatin structure and, foremost, dynamics occur in a spatiotemporal manner, we speculate that the interplay of chromatin structure and dynamics could involve a functional relationship (*28*): Transcriptional activity is closely linked to chromatin accessibility and the epigenomic state (*29*). Because chromatin structure and dynamics are related, dynamics could also correlate with transcriptional activity (*14*, *30*, *31*). However, it is currently unknown whether the structure-dynamics relationship revealed here is strictly mutual or whether it may be causal. Simulations hint that chromatin dynamics follows from structure (*22*, *23*); this question will be exciting to answer experimentally and in the light of active chromatin remodelers to elucidate a potential functional relationship to transcription. Chromatin regions that are switched from inactive to actively transcribing, for instance, undergo a structural reorganization accompanied by epigenetic modifications (*32*). The mechanisms driving recruitment of enzymes inducing histone modifications such as histone acetyltransferases, deacetylases, or methyltransferases are largely unknown but often involve the association to proteins (*33*). Their accessibility to the chromatin fiber is inter alia determined by local dynamics (*27*). Such a structure-dynamics feedback loop would constitute a quick and flexible way to transiently alter gene expression patterns upon reaction to external stimuli or to coregulate distant genes (*1*). Future work will study how structure-dynamics correlations differ in regions of different transcriptional activity and/or epigenomic states. Furthermore, probing the interactions between key transcriptional machines such as RNA polymerases with the local chromatin structure and recording their (possibly collective) dynamics could shed light into the target search and binding mechanisms of RNA polymerases with respect to the local chromatin structure. Deep-PALM in combination with optical flow paves the way to answer these questions by enabling the analysis of time-resolved super-resolution images of chromatin in living cells.

MATERIALS AND METHODS
Cell culture
Human osteosarcoma U2OS expressing H2B-PATagRFP cells were a gift from S. Huet (CNRS, UMR 6290, Institut Génétique et Développement de Rennes, Rennes, France); the histone H2B was cloned, as described previously (*34*). U2OS cells were cultured in Dulbecco's modified Eagle's medium [with glucose (4.5 g/liter)] supplemented with 10% fetal bovine serum (FBS), 2 mM glutamine, penicillin (100 μg/ml), and streptomycin (100 U/ml) in 5% CO_2 at 37°C. Cells were plated 24 hours before imaging on 35-mm petri dishes with a no. 1.5 coverslip-like bottom (ibidi, Biovalley) with a density of 2×10^5 cells per dish. Just before imaging, the growth medium

was replaced by Leibovitz's L-15 medium (Life Technologies) supplemented with 20% FBS, 2 mM glutamine, penicillin (100 μg/ml), and streptomycin (100 U/ml).

PALM imaging in living cells

Imaging of H2B-PAtagRFP in living U2OS cells was carried out on a fully automated Nikon Ti-E/B PALM (Nikon Instruments) microscope. The microscope is equipped with a full incubator enclosure with gas regulation to maintain a temperature of ~37°C for normal cell growth during live-cell imaging. Image sequences of 2000 frames were recorded with an exposure time of 30 ms per frame (33.3 frames/s). For Deep-PALM imaging, a relatively low power (~50 W/cm^2 at the sample) was applied for H2B-PATagRFP excitation at 561 nm and then combined with the 405 nm (~2 W/cm^2 at the sample) to photoactivate the molecules between the states. Note that for Deep-PALM imaging, switched fluorophores are not required to stay as long in the dark state as for conventional PALM imaging. We used oblique illumination microscopy (11) combined with total internal reflection fluorescence (TIRF) mode to illuminate a thin layer of 200 nm (axial resolution) across the nucleus. The reconstruction of super-resolved images improves the axial resolution only marginally (fig. S1, E and F). Laser beam powers were controlled by acoustic optic-modulators (AA Opto-Electronic). Both wavelengths were united into an oil immersion 1.49-NA (numerical aperture) TIRF objective (100×; Nikon). An oblique illumination was applied to acquire image series with a high signal-to-noise ratio. The fluorescence emission signal was collected by using the same objective and spectrally filtered by a Quad-Band beam splitter (ZT405/488/561/647rpc-UF2, Chroma Technology) with a Quad-Band emission filter (ZET405/488/561/647m-TRF, Chroma Technology). The signal was recorded on an electron-multiplying charge-coupled device camera (Andor iXon X3 DU-897, Andor Technology) with a pixel size of 108 nm. For axial correction, Perfect Focus System was applied to correct for defocusing. NIS-Elements software was used for acquiring the images.

PALM imaging and PALM data analysis in fixed cells

The same cell line (U2OS expressing H2B-PATagRFP), as in live-cell imaging, was used for conventional PALM imaging. Before fixation, cells were washed with phosphate-buffered saline (PBS) (three times for 5 min each) and then fixed with 4% paraformaldehyde (Sigma-Aldrich) diluted in PBS for 15 min at room temperature. A movie of 8000 frames was acquired with an exposure time of 30 ms per frame (33.3 frames/s). In comparison to Deep-PALM imaging, a relatively higher excitation laser of 561 nm (~60 W/cm^2 at the sample) was applied to photobleach H2B-PATagRFP and then combined with the 405 nm (~2.5 W/cm^2 at the sample) for photoactivating the molecules. We used the same oblique illumination microscopy combined with TIRF system, as applied in live-cell imaging.

PALM images from fixed cells were analyzed using ThunderSTORM (35). Super-resolution images were constructed by binning emitter localizations into 13.5 × 13.5 nm pixels and blurred by a Gaussian to match Deep-PALM images. The image segmentation was carried out as on images from living cells (see below).

Deep-PALM analysis

The CNN was trained using simulated data following Nehme et al. (15) for three labeling densities (4, 6, and 9 emitters/μm^2 per frame). Raw imaging data were checked for drift, as previously described

(12). The detected drift in raw images is in the range of <10 nm and therefore negligible. The accuracy of the trained net was evaluated by constructing ground truth images from the simulated emitter positions. The structural similarity index is computed to assess the similarity between reconstructed and ground truth images (36)

$$\text{SSIM} = \sum_{x,y} \frac{(2\mu_x\mu_x + C_1)(2\sigma_{xy} + C_2)}{(\mu_x^2 + \mu_y^2 + C_1)(\sigma_x^2 + \sigma_y^2 + C_2)} \quad (1)$$

where x and y are windows of the predicted and ground truth images, respectively, μ and σ denote their local means and SD, respectively, and σ_{xy} denotes their cross-variance. $C_1 = (0.01L)^2$ and $C_2 = (0.03L)^2$ are regularization constants, where L is the dynamic range of the input images. The second quantity to assess CNN accuracy is the root mean square error between the ground truth G and reconstructed image R

$$\text{RMSE} = \sqrt{\frac{1}{N}\sum_N (R - G)^2} \quad (2)$$

where N is the number of pixels in the images. After training, sequences of all experimental images were compared to the trained network, and predictions of single Deep-PALM images were summed to obtain a final super-resolved image. An up-sampling factor of 8 was used, resulting in an effective pixel size of 108 nm/8 = 13.5 nm. A blind/referenceless image spatial quality evaluator (37) was used to determine the optimal number of predictions to be summed. For visualization, super-resolved images were convolved with a Gaussian kernel (σ = 1 pixel) and represented using a false red, green, and blue colormap. The parameters of the three trained networks are available at https://github.com/romanbarth/DeepPALM-trained-models.

Fourier ring correlation analysis

Fourier ring correlation (FRC) is an unbiased method to estimate the spatial resolution in microscopy images. We follow an approach similar to the one described by Nieuwenhuizen et al. (38). For localization-based super-resolution techniques, the set of localizations is divided into two statistically independent subsets, and two images from these subsets are generated. The FRC is computed as the statistical correlation of the Fourier transforms of both sub-images over the perimeter of circles of constant frequency in the frequency domain. Deep-PALM, however, does not result in a list of localizations, but in predicted images directly. The set of 12 predictions from Deep-PALM were thus split into two statistically independent subsets, and the method described by Nieuwenhuizen et al. (38) was applied.

Chromatin blob identification

The super-resolved images displayed isolated regions of accumulated emitter density. To quantitatively assess the structural information implied by this accumulation of emitters in the focal plane, we developed a segmentation scheme that aims to identify individual blobs (fig. S3). A marker-assisted watershed segmentation was adapted to accurately determine blob boundaries. For this purpose, we use the raw predictions from the deep CNN without convolution (fig. S3A). The foreground in this image is marked by regional maxima and pixels with very high density (i.e., those with $I > 0.99 I_{max}$; fig. S3B). Since blobs are characterized by surrounding pixels of

considerably less density, the Euclidian distance transform is computed on the binary foreground markers. Background pixels (i.e., those pixels not belonging to any blobs) are expected to lie far away from any blob center, and thus, a good estimate for background markers are those pixels being furthest from any foreground pixel. We hence compute the watershed transform on the distance transform of foreground markers, and the resulting watershed lines depict background pixels (fig. S3C). Equipped with fore- and background markers (fig. S3D), we apply a marker-controlled watershed transform on the gradient of the input image (fig. S3E). The marker-controlled watershed imposes minima on marker pixels, preventing the formation of watershed lines across marker pixels. Therefore, the marker-controlled watershed accurately detects boundaries and blobs that might not have been previously marked as foreground (fig. S3F). Last, spurious blobs whose median- or mean intensity is below 10% of the maximum intensity are discarded, and each blob is assigned a unique label for further correspondence (fig. S3G). The area and centroid position are computed for each identified blob for further analysis. This automated segmentation scheme performs considerably better than other state-of-the-art algorithms for image segmentation because of the reliable identification of fore- and background markers accompanied by the watershed transform (note S1).

Chromatin blob properties
Centroid position, area, and eccentricity were computed. The eccentricity is computed by describing the blobs as an ellipse

$$E = \sqrt{1 - a^2/b^2} \tag{3}$$

where a and b are the short and long axes of the ellipse, respectively.

Chromatin blob identification from a computational chromatin model
We chose to use a computational chromatin model, recently introduced by Qi and Zhang (*19*), to elucidate the origin of experimentally determined chromatin blobs. Each bead of the model covers a sequence length of 5 kb and is assigned 1 of 15 chromatin states to distinguish promoters, enhancers, quiescent chromatin, etc. Starting from the simulated polymer configurations, we consider monomers within a 200-nm-thick slab through the center of the simulated chromosome. To generate super-resolved images as those from Deep-PALM analysis, fluorescence intensity is ascribed to each monomer. Monomer positions are subsequently discretized on a grid with 13.5-nm spacing and convolved with a narrow point-spread function, which results in images closely resembling experimental Deep-PALM images of chromatin. Chromatin blobs were then be identified and characterized as on experimental data (Fig. 2, A and B). Mapping back the association of each bead to a blob (if any) allows us to analyze principles of blob formation and maintenance using the distance and the association strength between each pair of monomers, averaged over all 20,000 simulated polymer configurations.

Radial distribution function
The radial distribution function $g(r)$ (also pair correlation function) is calculated (in two dimensions) by counting the number of blobs in an annulus of radius r and thickness dr. The result is normalized by the bulk density $\rho = n/A$, with the total number of blobs n and, A, the area of the nucleus, and the area of the annulus, $2\pi r\, dr$

$$dn(r) = \rho \cdot g(r) \cdot 2\pi r\, dr \tag{4}$$

Quantification of chromatin dynamics
Super-resolved images of chromatin showed spatially distributed blobs of varying size, but the resolved structure is too dense for state-of-the-art single-particle tracking methods to track. Furthermore are highly dynamic structures, assembling and dissembling within one to two super-resolved frames (Fig. 3D), which makes a single-particle tracking approach unsuitable. Instead, we used a method for dynamics reconstruction of bulk macromolecules with dense labeling, optical flow. Optical flow builds on the computation of flow fields between two successive frames of an image series. The integration of these flow fields from super-resolution images results in trajectories displaying the local motion of bulk chromatin with temporal and high spatial resolution. Further, the trajectories are classified into various diffusion models, and parameters describing the underlying motion are computed (*14*). Here, we use the effective diffusion coefficient D (in units of m^2/s^α), which reflects the magnitude of displacements between successive frames (the velocity of particles or monomers in the continuous limit) and the anomalous exponent α (*14*). The anomalous exponent reflects whether the diffusion is free ($\alpha = 1$, e.g., for noninteracting particles in solution), directed ($\alpha > 1$, e.g., as the result from active processes), or hindered ($\alpha < 1$, e.g., because of obstacles or an effective back-driving force). Furthermore, we compute the length of constraint L_c, which is defined as the SD of the trajectory positions with respect to its time-averaged position. Denoting $\boldsymbol{R}(t; \boldsymbol{R_0})$, the trajectory at time t originating from $\boldsymbol{R_0}$, the expression reads $L_c(\boldsymbol{R_0}) = \text{var}(\boldsymbol{R}(t; \boldsymbol{R_0}))^{1/2}$, where var denotes the variance. The length of constraint is a measure of the length scale explored of the monomer during the observation period. A complementary measure is the confinement level (*39*), which computes the inverse of the variance of displacements within a sliding window of length ω: $C \propto \omega/\text{var}(\boldsymbol{R}(t; \boldsymbol{R_0}))$, where the sliding window length is set to four frames (1.44 s). Larger values of C denote a more confined state than small ones.

Spatial correlation for temporally varying parameters
The NND and the area, as well as the flow magnitude, were calculated and assigned to the blobs' centroid position. To calculate the spatial correlation between parameters, the parameters were interpolated from the scattered centroid positions onto a regular grid spanning the entire nucleus. Because not every pixel in the original super-resolved images is assigned a parameter value, we chose an effective grid spacing of five pixels (67.5 nm) for the interpolated parameter maps. After interpolation, the spatial correlation was computed between parameter pairs: Let $\boldsymbol{r} = (x, y)^T$ denote a position on a regular two-dimensional grid and $f(\boldsymbol{r}, t)$ and $g(\boldsymbol{r}, t)$ two scalar fields with mean zero and variance one, at time t on that grid. The time series of parameter fields consist of N time points. The spatial cross-correlation between the fields f and g, which lie a lag time τ apart, is then calculated as

$$C(\boldsymbol{\rho}, \tau) = \frac{1}{N} \sum_t \frac{\sum_{x,y} f(\boldsymbol{r}, t) g(\boldsymbol{r} + \boldsymbol{\rho}, t + \tau)}{\sum_{x,y} f(\boldsymbol{r}, t) g(\boldsymbol{r}, t + \tau)} \tag{5}$$

where the space lag $\boldsymbol{\rho}$ is a two-dimensional vector $\boldsymbol{\rho} = (\Delta x, \Delta y)^T$. The sums in the numerator and denominator are taken over the spatial

dimensions; the first sum is taken over time. The average is thus taken over all time points that are compliant with time lag τ. Subsequently, the radial average in space is taken over the correlation, thus effectively calculating the spatial correlation $C(\rho, \tau)$ over the space lag $\rho = \sqrt{\Delta x^2 + \Delta y^2}$. If $f = g$, then the spatial autocorrelation is computed.

Spatial correlation for static parameters

We denote as global parameters those that reflect the structural and dynamic behavior of chromatin spatially resolved in a time-averaged manner. Examples involve the diffusion constant, the anomalous exponent, the length of constraint, but also time-averaged NND maps, etc. (fig. S8). Those parameters are useful to determine time-universal characteristics. The spatial correlation between those parameters is equivalent to the expression given for temporally varying parameters when the temporal dimension is omitted, effectively resulting in a correlation curve $C(\rho)$.

t-distributed stochastic neighbor embedding

The distance from the periphery, intensity, their NND, area, flow magnitude, and confinement level of each identified blob form the six-dimensional–input feature space for t-SNE analysis. The parameters for each blob ($n = 3{,}260{,}232$; divided into subsets of approximately 10,000) were z-transformed before the t-SNE analysis. The t-SNE analysis was performed using MATLAB and the Statistics and Machine Learning Toolbox (Release 2017b; The MathWorks Inc., Natick, MA, USA) with the Barnes-Hut approximation. The algorithm was tested using different distance metrics and perplexity values and showed robust results within the examined ranges (note S3 and fig. S10).

SUPPLEMENTARY MATERIALS

Supplementary material for this article is available at http://advances.sciencemag.org/cgi/content/full/6/27/eaaz2196/DC1

View/request a protocol for this paper from *Bio-protocol*.

REFERENCES AND NOTES

1. B. van Steensel, E. E. M. Furlong, The role of transcription in shaping the spatial organization of the genome. *Nat. Rev. Mol. Cell Biol.* **20**, 327–337 (2019).
2. E. Lieberman-Aiden, N. L. van Berkum, L. Williams, M. Imakaev, T. Ragoczy, A. Telling, I. Amit, B. R. Lajoie, P. J. Sabo, M. O. Dorschner, R. Sandstrom, B. Bernstein, M. A. Bender, M. Groudine, A. Gnirke, J. Stamatoyannopoulos, L. A. Mirny, E. S. Lander, J. Dekker, Comprehensive mapping of long-range interactions reveals folding principles of the human genome. *Science* **326**, 289–293 (2009).
3. E. H. Finn, G. Pegoraro, H. B. Brandão, A.-L. Valton, M. E. Oomen, J. Dekker, L. Mirny, T. Misteli, Extensive heterogeneity and intrinsic variation in spatial genome organization. *Cell* **176**, 1502–1515.e10 (2019).
4. J. R. Dixon, S. Selvaraj, F. Yue, A. Kim, Y. Li, Y. Shen, M. Hu, J. S. Liu, B. Ren, Topological domains in mammalian genomes identified by analysis of chromatin interactions. *Nature* **485**, 376–380 (2012).
5. B. Bintu, L. J. Mateo, J.-H. Su, N. A. Sinnott-Armstrong, M. Parker, S. Kinrot, K. Yamaya, A. N. Boettiger, X. Zhuang, Super-resolution chromatin tracing reveals domains and cooperative interactions in single cells. *Science* **362**, eaau1783 (2018).
6. M. A. Ricci, C. Manzo, M. F. García-Parajo, M. Lakadamyali, P. M. Cosma, Chromatin fibers are formed by heterogeneous groups of nucleosomes in vivo. *Cell* **160**, 1145–1158 (2015).
7. K. Fang, X. Chen, X. Li, Y. Shen, J. Sun, D. M. Czajkowsky, Z. Shao, Super-resolution imaging of individual human subchromosomal regions in situ reveals nanoscopic building blocks of higher-order structure. *ACS Nano* **12**, 4909–4918 (2018).
8. E. Miron, R. Oldenkamp, D. M. S. Pinto, J. M. Brown, A. R. Carvalho Faria, H. A. Shaban, J. D. P. Rhodes, C. Innocent, S. de Ornellas, V. Buckle, L. Schermelleh, Chromatin arranges in filaments of blobs with nanoscale functional zonation. *bioRxiv* doi.org/10.1101/566638 (2019).
9. J. Xu, H. Ma, J. Jin, S. Uttam, R. Fu, Y. Huang, Y. Liu, Super-resolution imaging of higher-order chromatin structures at different epigenomic states in single mammalian cells. *Cell Rep.* **24**, 873–882 (2018).
10. A. N. Boettiger, B. Bintu, J. R. Moffitt, S. Wang, B. J. Beliveau, G. Fudenberg, M. Imakaev, L. A. Mirny, C.-T. Wu, X. Zhuang, Super-resolution imaging reveals distinct chromatin folding for different epigenetic states. *Nature* **529**, 418–422 (2016).
11. T. Nozaki, R. Imai, M. Tanbo, R. Nagashima, S. Tamura, T. Tani, Dynamic organization of chromatin domains revealed by super-resolution live-cell imaging. *Mol. Cell* **10**, 1–12 (2017).
12. H. A. Shaban, R. Barth, K. Bystricky, Formation of correlated chromatin domains at nanoscale dynamic resolution during transcription. *Nucleic Acids Res.* **46**, e77 (2018).
13. W. Xiang, M. J. Roberti, J.-K. Hériché, S. Huet, S. Alexander, J. Ellenberg, Correlative live and super-resolution imaging reveals the dynamic structure of replication domains. *J. Cell Biol.* **217**, 1973–1984 (2018).
14. H. A. Shaban, R. Barth, L. Recoules, K. Bystricky, Hi-D: nanoscale mapping of nuclear dynamics in single living cells. *Genome Biol.* **21**, 95 (2020).
15. E. Nehme, L. E. Weiss, T. Michaeli, Y. Shechtman, Deep-STORM: Super-resolution single-molecule microscopy by deep learning. *Optica.* **5**, 458–464 (2018).
16. H. Shroff, C. G. Galbraith, J. A. Galbraith, E. Betzig, Live-cell photoactivated localization microscopy of nanoscale adhesion dynamics. *Nat. Methods* **5**, 417–423 (2008).
17. Q. Szabo, D. Jost, J.-M. M. Chang, D. I. Cattoni, G. L. Papadopoulos, B. Bonev, T. Sexton, J. Gurgo, C. Jacquier, M. Nollmann, F. Bantignies, G. Cavalli, TADs are 3D structural units of higher-order chromosome organization in *Drosophila*. *Sci. Adv.* **4**, eaar8082 (2018).
18. R. J. Marsh, K. Pfisterer, P. Bennett, L. M. Hirvonen, M. Gautel, G. E. Jones, S. Cox, Artifact-free high-density localization microscopy analysis. *Nat. Methods* **15**, 689–692 (2018).
19. Y. Qi, B. Zhang, Predicting three-dimensional genome organization with chromatin states. *PLOS Comput. Biol.* **15**, e1007024 (2019).
20. H. D. Ou, S. Phan, T. J. Deerinck, A. Thor, M. H. Ellisman, C. C. O'Shea, ChromEMT: Visualizing 3D chromatin structure and compaction in interphase and mitotic cells. *Science* **357**, eaag0025 (2017).
21. J. Kind, L. Pagie, H. Ortabozkoyun, S. Boyle, S. S. de Vries, H. Janssen, M. Amendola, L. D. Nolen, W. A. Bickmore, B. van Steensel, Single-cell dynamics of genome-nuclear lamina interactions. *Cell* **153**, 178–192 (2013).
22. M. Di Pierro, D. A. Potoyan, P. G. Wolynes, J. N. Onuchic, Anomalous diffusion, spatial coherence, and viscoelasticity from the energy landscape of human chromosomes. *Proc. Natl. Acad. Sci. U.S.A.* **115**, 7753–7758 (2018).
23. L. Liu, G. Shi, D. Thirumalai, C. Hyeon, Chain organization of human interphase chromosome determines the spatiotemporal dynamics of chromatin loci. *PLOS Comput. Biol.* **14**, e1006617 (2018).
24. A. Rosa, R. Everaers, Structure and dynamics of interphase chromosomes. *PLOS Comput. Biol.* **4**, e1000153 (2008).
25. L. Van der Maaten, G. Hinton, Visualizing data using t-SNE. *J. Machine Learning Res.* **9**, 2579–2605 (2008).
26. K. E. Polovnikov, M. Gherardi, M. Cosentino-Lagomarsino, M. V. Tamm, Fractal folding and medium viscoelasticity contribute jointly to chromosome dynamics. *Phys. Rev. Lett.* **120**, 088101 (2018).
27. S. Hihara, C.-G. Pack, K. Kaizu, T. Tani, T. Hanafusa, T. Nozaki, S. Takemoto, T. Yoshimi, H. Yokota, N. Imamoto, Y. Sako, M. Kinjo, K. Takahashi, T. Nagai, K. Maeshima, Local nucleosome dynamics facilitate chromatin accessibility in living mammalian cells. *Cell Rep.* **2**, 1645–1656 (2012).
28. L. Giorgetti, R. Galupa, E. P. Nora, T. Piolot, F. Lam, J. Dekker, G. Tiana, E. Heard, Predictive polymer modeling reveals coupled fluctuations in chromosome conformation and transcription. *Cell* **157**, 950–963 (2014).
29. S. M. Görisch, M. Wachsmuth, K. F. Tóth, P. Lichter, K. Rippe, Histone acetylation increases chromatin accessibility. *J. Cell Sci.* **118**, 5825–5834 (2005).
30. T. Germier, S. Kocanova, N. Walther, A. Bancaud, H. A. Shaban, H. Sellou, A. Z. Politi, J. Ellenberg, F. Gallardo, K. Bystricky, Real-time imaging of a single gene reveals transcription-initiated local confinement. *Biophys. J.* **113**, 1383–1394 (2017).
31. R. Nagashima, K. Hibino, S. S. Ashwin, M. Babokhov, S. Fujishiro, R. Imai, T. Nozaki, S. Tamura, T. Tani, H. Kimura, M. Shribak, M. T. Kanemaki, M. Sasai, K. Maeshima, Single nucleosome imaging reveals loose genome chromatin networks via active RNA polymerase II. *J. Cell Biol.* **218**, 1511–1530 (2019).
32. N. Soshnikova, D. Duboule, Epigenetic temporal control of mouse *Hox* genes in vivo. *Science* **324**, 1320–1323 (2009).
33. M. Laisné, N. Gupta, O. Kirsh, S. Pradhan, P.-A. Defossez, Mechanisms of DNA methyltransferase recruitment in mammals. *Genes* **9**, 617 (2018).
34. H. Sellou, T. Lebeaupin, C. Chapuis, R. Smith, A. Hegele, H. R. Singh, M. Kozlowski, S. Bultmann, A. G. Ladurner, G. Timinszky, S. Huet, The poly(ADP-ribose)–dependent

chromatin remodeler Alc1 induces local chromatin relaxation upon DNA damage. *Mol. Biol. Cell* **27**, 3791–3799 (2016).

35. M. Ovesný, P. Křížek, J. Borkovec, Z. Švindrych, G. M. Hagen, ThunderSTORM: A comprehensive ImageJ plug-in for PALM and STORM data analysis and super-resolution imaging. *Bioinformatics* **30**, 2389–2390 (2014).

36. Z. Wang, A. C. Bovik, H. R. Sheikh, E. P. Simoncelli, Image quality assessment: From error visibility to structural similarity. *IEEE Trans. Image Process.* **13**, 600–612 (2004).

37. A. Mittal, A. K. Moorthy, A. C. Bovik, No-reference image quality assessment in the spatial domain. *IEEE Trans. Image Process.* **21**, 4695–4708 (2012).

38. R. P. J. Nieuwenhuizen, K. A. Lidke, M. Bates, D. L. Puig, D. Grünwald, S. Stallinga, B. Rieger, Measuring image resolution in optical nanoscopy. *Nat. Methods* **10**, 557–562 (2013).

39. A. Sergé, N. Bertaux, H. Rigneault, D. Marguet, Dynamic multiple-target tracing to probe spatiotemporal cartography of cell membranes. *Nat. Methods* **5**, 687–694 (2008).

40. S. S. P. Rao, M. H. Huntley, N. C. Durand, E. K. Stamenova, I. D. Bochkov, J. T. Robinson, A. L. Sanborn, I. Machol, A. D. Omer, E. S. Lander, E. L. Aiden, A 3D map of the human genome at kilobase resolution reveals principles of chromatin looping. *Cell* **159**, 1665–1680 (2014).

41. W. M. Rand, Objective criteria for the evaluation of clustering methods.. *J. Am. Stat. Assoc.* **66**, 846–850 (1971).

42. S. Beucher, B. Marcotegui, B. P. Marcotegui, P algorithm, a dramatic enhancement of the waterfall transformation (2009); https://hal-mines-paristech.archives-ouvertes.fr/hal-00835019.

Citation: R. Barth, K. Bystricky, H. A. Shaban, Coupling chromatin structure and dynamics by live super-resolution imaging. *Sci. Adv.* **6**, eaaz2196 (2020).

Science Advances

Coupling chromatin structure and dynamics by live super-resolution imaging

R. Barth, K. Bystricky and H. A. Shaban

ARTICLE TOOLS	http://advances.sciencemag.org/content/6/27/eaaz2196
SUPPLEMENTARY MATERIALS	http://advances.sciencemag.org/content/suppl/2020/06/29/6.27.eaaz2196.DC1
REFERENCES	This article cites 40 articles, 10 of which you can access for free http://advances.sciencemag.org/content/6/27/eaaz2196#BIBL
PERMISSIONS	http://www.sciencemag.org/help/reprints-and-permissions

Use of this article is subject to the Terms of Service